ORIGINAL PAPER

Interactions of ferro-nanoparticles (hematite and magnetite) with reservoir sandstone: implications for surface adsorption and interfacial tension reduction

Abdullah Musa Ali[1,2] · Noorhana Yahya[1] · Saima Qureshi[1]

Abstract

There are a few studies on the use of ferro-nanofluids for enhanced oil recovery, despite their magnetic properties; hence, it is needed to study the adsorption of iron oxide (Fe_2O_3 and Fe_3O_4) nanoparticles (NPs) on rock surfaces. This is important as the colloidal transport of NPs through the reservoir is subject to particle adsorption on the rock surface. Molecular dynamics simulation was used to determine the interfacial energy (strength) and adsorption of Fe_2O_3 and Fe_3O_4 nanofluids infused in reservoir sandstones. Fourier transform infrared spectroscopy and X-ray photon spectroscopy (XPS) were used to monitor interaction of silicate species with Fe_2O_3 and Fe_3O_4. The spectral changes show the variation of dominating silicate anions in the solution. Also, the XPS peaks for Si, C and Fe at 190, 285 and 700 eV, respectively, are less distinct in the spectra of sandstone aged in the Fe_3O_4 nanofluid, suggesting the intense adsorption of the Fe_3O_4 with the crude oil. The measured IFT for brine/oil, Fe_2O_3/oil and Fe_3O_4/oil are 40, 36.17 and 31 mN/m, respectively. Fe_3O_4 infused with reservoir sandstone exhibits a higher silicate sorption capacity than Fe_2O_3, due to their larger number of active surface sites and saturation magnetization, which accounts for the effectiveness of Fe_3O_4 in reducing IFT.

Keywords Magnetite and hematite nanoparticles · Rock surface adsorption · Molecular dynamics simulation · Interfacial tension (IFT)

1 Introduction

The main magnetic molecules in the ferro-nanofluid group are Fe_3O_4 (magnetite), α-Fe_2O_3 (hematite, weakly ferromagnetic or antiferromagnetic), γ-Fe_2O_3 (maghemite, ferrimagnetic), FeO (wüstite, antiferromagnetic), ε-Fe_2O_3 and β-Fe_2O_3 (Negin et al. 2016; Tsai et al. 2010; Wu et al. 2008). Huh et al. (2015) reported that ferrofluids comprise

hydrophobic magnetic, paramagnetic or superparamagnetic iron oxide nanoparticles (NPs). Iron oxide (Fe_2O_3/Fe_3O_4) NPs can increase the viscosity of the displacing fluid, resulting in higher sweep efficiency, which is important since most sandstone reservoirs act as neutral or preferentially oil-wet due to adsorption of acidic component of crude oil on their surfaces (Buckley and Liu 1998; Rezaei Gomari et al. 2006). The concept of using ferro-nanofluids was introduced in enhanced oil recovery (EOR)-related processes by Kothari et al. (2010), where they reported that iron oxide NPs are able to reduce viscosity. Kothari et al. (2010) reported that ferro-nanofluids reduce interfacial tension (IFT) in both oil-wet and water-wet reservoirs by causing the collapse of isolated oil bubbles confined in the centre of the pores. Kothari et al. (2010) further hypothesized that the alignment of the reservoir fluid molecules due to the presence of dipole moment reduces flow resistance, possibly leading to higher recovery. Iron oxide NPs have revealed minimal retention in porous media, as shown by a wide-ranging run of transport experiments, which were validated by modelling studies (Yu et al. 2010; Zhang et al. 2015, 2016). However, the research

---

Edited by Yan-Hua Sun

✉ Abdullah Musa Ali
  alicorp@yahoo.com

  Noorhana Yahya
  norhana.yahya@utp.edu.my

  Saima Qureshi
  saima_qureshi02@utp.edu.my

[1] Universiti Teknologi PETRONAS, 32610 Seri Iskandar, Perak, Malaysia

[2] Geology Department, Bayero University, Kano, Kano, Nigeria

Ⓐ Springer

was limited to the rheological properties of the ferrofluid without investigating the direct application of this fluid in EOR processes.

Haroun et al. (2012) achieved an ultimate recovery of 57% using Fe_2O_3 NPs on carbonate core plugs, while Ogolo et al. (2012) reported an additional recovery up to 24% using Fe_2O_3 NPs dispersed in water. After conducting additional experiments, Ogolo et al. (2012) suggested that iron oxide, when dispersed in brine, performs as a practically good EOR agent in sandstone reservoirs. In addition, Joonaki and Ghanaatian (2014) reported that Fe_2O_3 were only able to recover 17% extra oil, while other NPs (i.e. Al_2O_3 and SiO_2) recovered around 20% additional oil. However, Kamal et al. (2017) suggested that more experimental work is required to understand the underlying mechanism of improvement in interfacial properties using iron oxide NPs. Experimental studies that have been carried out in this area largely dealt with determining the optimum NPs concentrations corresponding to minimum IFT. Despite the several studies of the effectiveness of nanofluids in reducing IFT (Hendraningrat et al. 2013; Li et al. 2013; Parvazdavani et al. 2014; Torsater et al. 2012), there is a dearth of research on the potential use of iron oxides for EOR. The mechanisms by which iron oxide (Fe_2O_3 and Fe_3O_4) NPs interact with sandstone to influence reservoir properties are not thoroughly understood (Agista et al. 2018). Given that rock–fluid interactions and IFT play a significant role in oil recovery methods, it is crucial to explore interactions of ferro-nanofluids with reservoir rock to determine the optimum mechanisms for increasing oil recovery. The interfacial reaction between silicates in a reservoir system and iron oxide surfaces is of great importance in nanofluid recovery, since IFT and wettability modifications are dependent on adsorption reactions between the ferric species and the silicates in the reservoir sandstone.

NPs are basically used in EOR operations because of their wettability alteration and IFT reduction capabilities (Soleimani et al. 2018). The colloidal transport of the NPs through the reservoir is subject to particle adsorption on the rock surface, which in turn is controlled by surface charges of the NPs (Dunphy Guzman et al. 2006). In addition, wettability alteration is dependent on adsorption of the nanoparticles on the surfaces of the sandstone grains. Moreover, studies of crude oil adsorption are valuable in directing the oil-displacing agent design and oil exploitation. Hence, there is need to determine possible adsorption as well as the respective adsorption energies of Fe_2O_3 and Fe_3O_4 NPs on the rock surface. Molecular dynamics (MD) simulation was used to determine the interfacial energy (strength) and adsorption configurations of selected ferro-nanofluids (Fe_2O_3 and Fe_3O_4) infused with reservoir sandstones. The density functional theory (DFT) calculation is a multifaceted technique to predict various energetic, structural and electronic properties of diverse systems, thus providing theoretical direction

for relevant experimental studies. Spectroscopic techniques such as attenuated total reflection Fourier transform infrared (ATR-FTIR) and X-ray photon spectroscopy (XPS) were used to monitor possible transformations and band shifts in the silicate and C–H species. The adsorption and IFT of Fe_2O_3 and Fe_3O_4 nanofluids were comparatively analysed to determine the better iron species. In general, this study outlines the mechanisms involved in the sorption of Fe_2O_3 and Fe_3O_4 nanofluids onto sandstone surfaces, with respect to EOR.

2 Materials and methods

To evaluate the interactions of ferro-nanofluids with reservoir sandstone, some simulation and experimental studies were carried out. Both approaches are discussed in the underlying subsections.

2.1 Molecular dynamics simulation of adsorption of Fe_2O_3 and Fe_3O_4 NPs on reservoir sandstone surfaces

The adsorption of the selected Fe_2O_3 and Fe_3O_4 NPs in addition to their effects on the shear viscosity of oil was simulated on an atom-based model using the dynamic Forcite tool in the Material Studio software at varying pressures. Molecular dynamics simulation in Material Studio software was applied to simulate the adsorption force between reservoir rock surfaces and molecules of the ferro-nanofluids. Berea sandstone of 24% porosity and bulk composition of quartz, feldspar and kaolinite were used. Specific steps were taken to construct the reservoir sandstone. In step 1, the initial structures of sandstone components (quartz, feldspar and kaolinite) were separately constructed (Fig. 1), and then geometrically optimized to reduce the magnitude of calculated force until they become smaller than defined convergence tolerances (Khaled 2012). An amorphous cell was built. The sandstone components were subsequently imported into the amorphous cell with compositions of 78%, 5%, 5%, 5% and 7% for quartz, anorthite, orthoclase, albite and kaolinite, respectively. In step 2, C_8H_{18} (clusters of hexane) and brine ($H_2O + NaCl$) were incorporated into the cell containing the preconditioned mineral surface to closely replicate the reservoir environment (Fig. 1). For step 3, the shared orientation between the oil and the nanoparticle surface was arbitrarily selected, with the oil components placed into a box with same length and width to silica surface. In the course of the simulation, the quartz surfaces were fixed since the vibration of these atoms was minute at room temperature and could be disregarded.

The following scenario involves the adsorption of the ferro-nanofluids on the reservoir sandstone. Prior to the
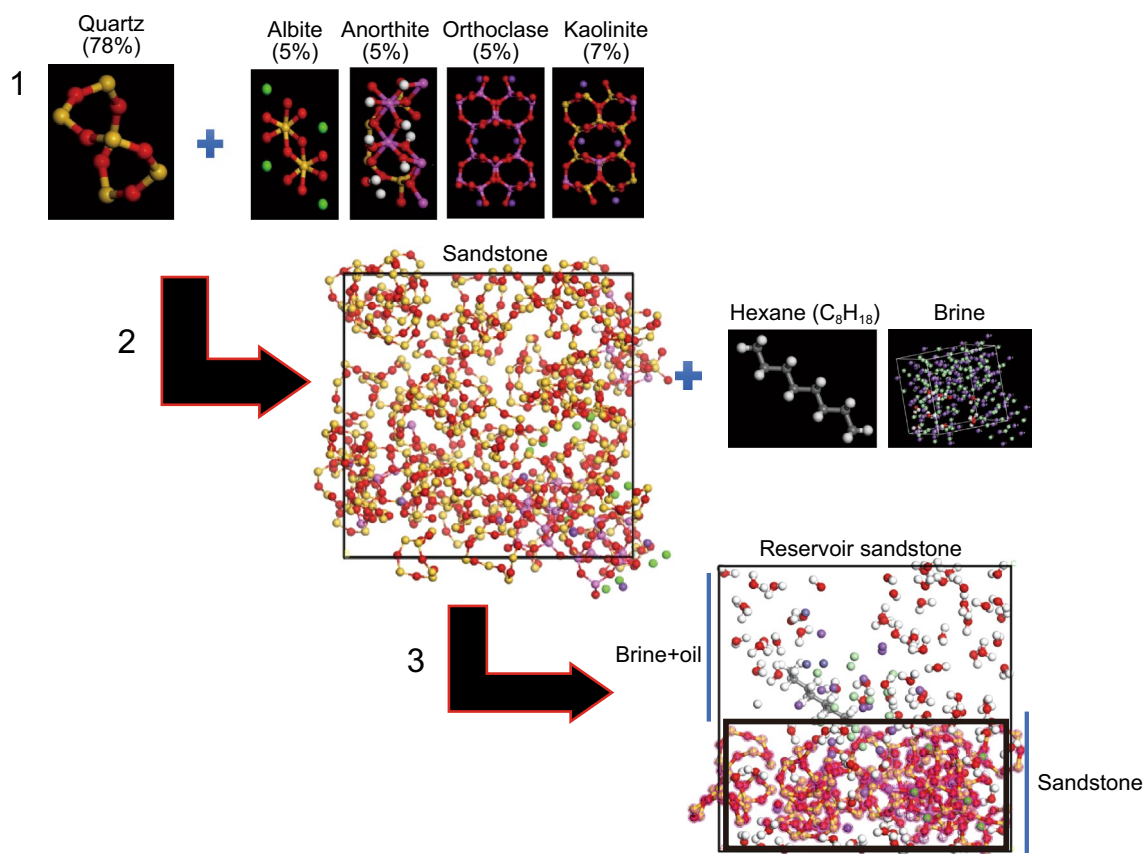
Fig. 1 Procedural steps for constructing reservoir sandstone in Material Studio. Sandstone components of quartz, feldspar and kaolinite were constructed. Hexane (C_8H_{18}) and brine, representing reservoir fluids, were infused into the sandstone to create a realistic scenario of sandstone reservoir

adsorption configuration, the amorphous cell was transformed into a super cell of $5 \times 3 \times 1$ with dimensions of 2.46 nm $\times$ 2.55 nm $\times$ 1.41 nm and three-dimensional periodic boundary conditions, and a vacuum slab was created afterwards. Similarly, the adsorption comprises specific steps. Firstly, nanofluids of Fe_2O_3 and Fe_3O_4 nanoparticles with diameter of 4 Å were built to form the adsorbates. In step 2, the adsorbate was imported to the vacuum slab, and the target atoms were marked (Fig. 2). For step 3, the NPs were placed at the centre of the cubic simulation cell to ensure full dispersion in the reservoir sandstone. A single run from nanoparticle optimization to adsorption took about 72 h. The simulations were performed using the supercell scheme. All NPs and oil chains were fully optimized until the maximum force acting on any atom was lower than 0.001 eV/A.

Due to the presence of the NPs, a universal force field was applied rather than the COMPASS force field. The Materials Studio software comprises a full implementation of the universal force field, including bond order assignment. The adsorption module was then run to create a combined adsorbent–adsorbate structure. The adsorption locator module simulates the reservoir sandstone substrate loaded with the adsorbates of fixed composition. The preferential adsorption sites on the cleaved sandstone surface are targeted by finding the low-energy adsorption sites. The adsorption energies of the nanofluids on the sandstone in the presence of brine and oil were measured using the adsorption configuration locator. The total energy and energy distribution of the adsorption were calculated for the different adsorbates. The energy calculation combines the bonding (stretching, bending, torsion energy and the diagonal and off-diagonal cross-coupling terms) and nonbonding terms. The van der Waals interactions are condensed at $r_c = 12$ Å by executing a spline function from 11 Å. The Coulomb interactions are calculated via Ewald summation (Allen and Tildesley 1996). The interactions between the NPs and the reservoir sandstone surface are simply intramolecular and van der Waals types. Nonetheless, the intramolecular Coulomb interactions were subjected to Ewald summation in preference to the cut-off method. To properly describe the on-site Coulomb interactions in the localized $3d$ orbitals of strongly correlated systems, additional Hubbard-type terms were included. All calculations are spin-polarized computations. London dispersion interactions were included in the total bonding energy. Prior to the MD simulations, energy
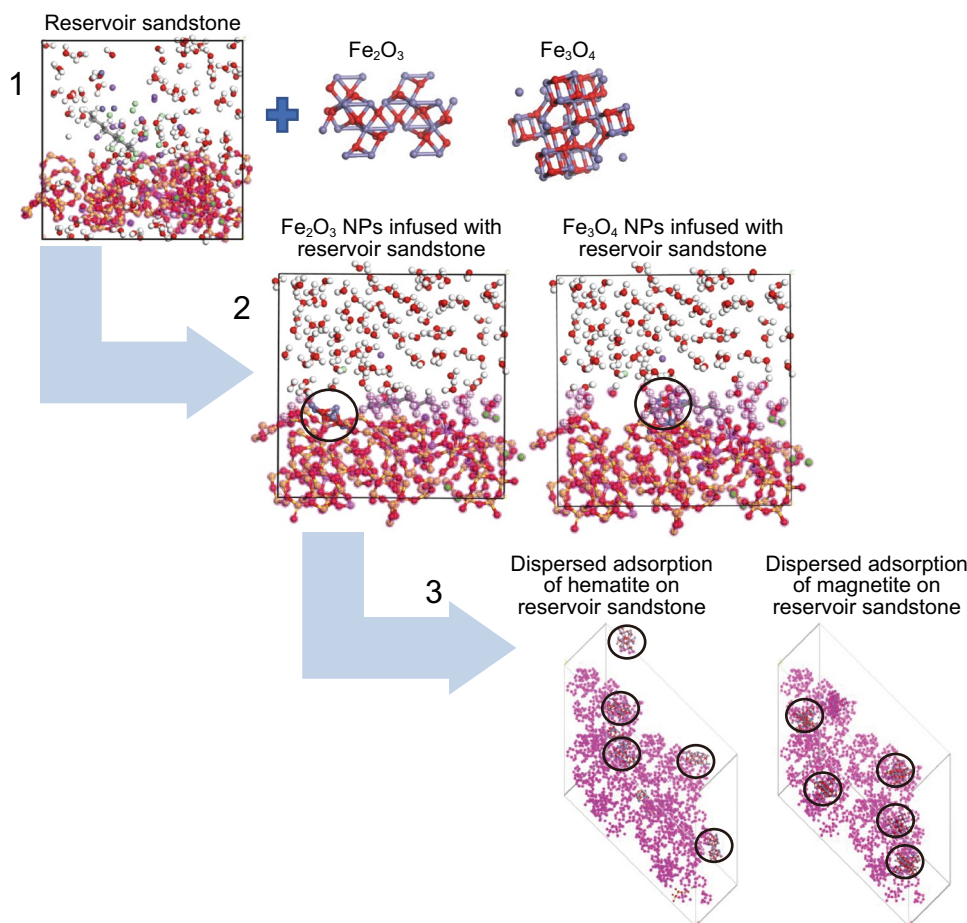
Fig. 2 **Step 1** Geometrically optimized reservoir sandstone model and Fe_2O_3 and Fe_3O_4 nanostructures; **Step 2** the basic hybrid model of a porous medium (reservoir sandstone) with oil (C_8H_{18}) and brine infused with Fe_2O_3 and Fe_3O_4 nanostructures; **Step 3** orthogonal view of the geometrically optimized models of configurations of Fe_2O_3 and Fe_3O_4 nanostructures (indicated by black circles) dispersed in the reservoir sandstone

minimizations were done to relax the local unfavourable structure of the NPs. The surface energy of the oil adsorbed on the sandstone was also determined. The volume of adsorbates was expanded to ensure complete dispersion on the sandstone surface. The stress autocorrelation function (SACF), also referred to as pressure correlation function, was used to estimate the shear viscosity of the reservoir fluid with the incorporation of Fe_2O_3 and Fe_3O_4. Several simulations were performed to fully relax the system, and the trajectories of the final run were selected for analysis.

2.2 Stability of interaction: interfacial energy

The binding energy per atom was used as the measure of the stability of the studied systems. It was calculated according to the equation:

$$E_{b/N} = \frac{1}{N}\left(E_{tot}^{model} - \sum_{\alpha=1}^{N} E_{atom}^{\alpha}\right) \tag{1}$$

where N is the number of atoms in the system, and E_{atom}^{α} is the total atomic energy of the free atom of type α (H, C, O, Si, Fe). More stable systems are characterized by more negative $E_{b/N}$.

To further evaluate the strength of interaction between the NPs and oil or water molecules inside pores, the interaction energy was defined. The relative energy of interactions between those components of the system can be described as:

$$E_{int} = E_{tot}^{system} - \sum_{i=1}^{n} E_{tot}^{comp,i} + E_{corr} \tag{2}$$

where E_{tot}^{system} and $E_{tot}^{comp,i}$ are the total energies of investigated system and all isolated components in the pore. E_{corr} is the

basis set superposition error (BSSE) correction due to the usage of numerical code with a localized basis.

The interfacial strength is defined as:

$$\gamma = \frac{-E_{\text{tot}}^{\text{model}} - E_{\text{tot}}^{\text{sandstone}} - \sum_{i=1}^{N} E_{\text{tot}}^{\text{comp},i}}{A_{\text{cavity}}} \quad (3)$$

where $E_{\text{tot}}^{\text{model}}$, $E_{\text{tot}}^{\text{sandstone}}$, $E_{\text{tot}}^{\text{comp},i}$ are the total energies of the hybrid model, sandstone and all components in the cavity such as oil and NP, respectively. The interfacial area, A_{cavity}, is the total surface area of the cavity calculated as solvent-exposed surface area of cavity in sandstone part of the model. High γ value indicates the strong bonding between oil and porous medium, while low γ value suggests increasing separation tendencies in the system. In order to quantify morphology changes of the interface after addition of the chosen nanostructures into the system, the interfacial strength is defined as in Eq. (4).

$$\gamma = -\frac{E_{\text{tot}}^{\text{model}} - E_{\text{tot}}^{\text{sandstone}} - \sum_{i=1}^{N} E_{\text{tot}}^{\text{comp},i}}{A_{\text{surface}}} \quad (4)$$

where A_{surface} is the total surface area of the grain calculated as solvent-exposed surface area of quartz grain.

2.3 Experimental section

A series of experiments were performed to explore the interactions between iron oxide (Fe_2O_3/Fe_3O_4) NPs and sandstone in the presence of brine and crude oil. The experiments were conducted using a Berea core sandstone. Brine (NaCl solution) with salinity of 11,000 ppm was prepared to reflect the concentration of infiltrated and connate water in the offshore sandstone reservoir. The Fe_2O_3 and Fe_3O_4 NPs were purchased from Sigma-Aldrich. The NPs (0.5 g each) were dispersed in brine (100 mL) to attain 0.05 wt% of nanofluids. The sandstone core was first aged in the brine for 5 days at 110 °C using the hydrothermal synthesis autoclave reactor, which consists of airtight Teflon reaction vessels and has a working pressure of ≤ 3 MPa or 30 bars, to create spontaneous imbibition. The core was then extracted and subsequently aged in crude oil for another 5 days using the same autoclave. After that, the prepared nanofluids were added to the Teflon vessel holding the sore sample. The saturated samples were further aged in the autoclave for 2 weeks to allow interactions among respective components (brine, crude oil and nanofluids). The plain and saturated Berea core samples are shown in Fig. 3. Afterwards, the samples were dried in an oven set at 60 °C for 2 days and slowly crushed in an agate mortar to increase the exposed surface area, before conducting the characterizations. All glassware and parts of the instrument in contact with the samples were carefully
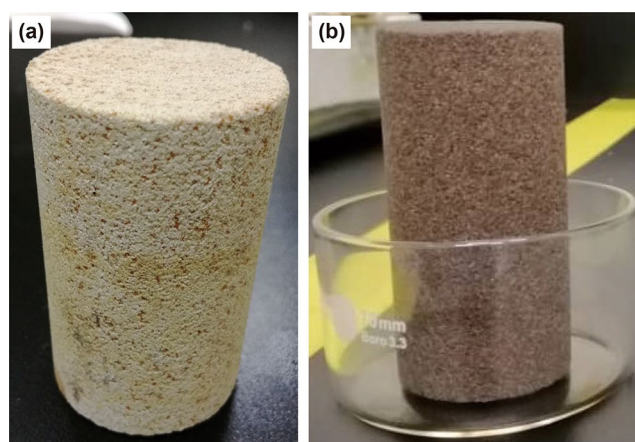
Fig. 3 **a** Berea core samples. **b** Berea core sample saturated with brine, crude oil, and nanofluids

cleaned with different standard procedures, depending on the materials, to avoid any contamination.

The morphological characterization and surface composition analysis of the samples was performed using a high-resolution field emission scanning electron microscope (FESEM: Carl Zeiss Supra 55VP; operated at 5–20 kV). FTIR spectra were used for composition analysis and to identify disparity in chemical bonds. This method is based on the interaction between infrared (IR) electromagnetic radiation and the vibrational motion of atomic clusters. FTIR spectra were recorded at room temperature using a Shimadzu FTIR 8400S, which was linked to a desktop computer loaded with the software, labsolutions IR, to process the recorded spectra. XPS was used to determine the composition, chemical state of elements and depth profiling using the X-ray beam and measuring energy of electrons emitted from the surface of the material. The model of XPS used in this study is the Thermo Scientific K-Alpha equipment, a fully integrated, monochromated small-spot XPS system with depth profiling capabilities. The base pressure was below 10–8 mbar. Data collection was accomplished with a microprocessor interfaced to a PC computer. IFT measurements were carried out using a DCAT tensiometer at room temperature to determine possible variations in surface tension in the liquid/liquid phases of brine/crude oil, Fe_2O_3 NPs/crude oil and Fe_3O_4 NPs/crude oil. The equipment employs the Wilhelmy plate method for IFT measurements, which involves the use of a vertically suspending plate to touch the liquid surface or interface; then, a force that correlates the IFT to contact angle, acts on this plate. A vibrating sample magnetometer (VSM) was used to obtain the saturation magnetization of the iron oxide nanoparticles.

3 Results

3.1 Simulation

3.1.1 Adsorption energy

Molecular dynamics simulations are applied to explore the adsorption process of the single- and double-chained magnetite and hematite on SiO_2 and other silicate surfaces present in the reservoir sandstone. The total adsorption energy was calculated, which is inclusive of binding, intramolecular and isolated molecular energies. After 10 iterative steps, the adsorption energy for magnetite NPs is about 100 kcal/mol, while that of Fe_2O_3 NPs is approximately -2300 kcal/mol
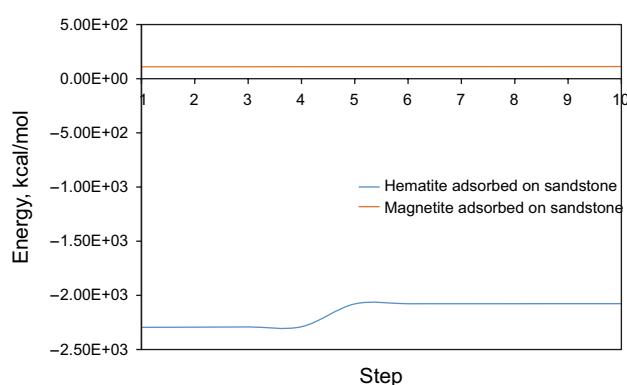

Fig. 4 Adsorption energy plots for the hematite and magnetite NPs onto reservoir sandstone

(Fig. 4). The adsorption difference is reflective of surface-structural variations in the adsorbates, adsorbents and interfaces in Fe_2O_3 and Fe_3O_4 interactions with the sandstone. The relatively large adsorption energies for both NPs infused with the reservoir sandstone can be attributed to their high molecular weight and reduced long-range diffusion of the inherent hydrodynamic interactions, as well as interaction between the oxygen atoms in Fe_2O_3 and Fe_3O_4 compounds and SiO_2 surface. The negative energy of Fe_2O_3 is indicative of exothermic adsorption reaction and implies that the adsorption structures are stable. Here, the adsorption leads to decreased residual forces on the SiO_2 surface, which in turn initiates a decline in the surface energy. The negative value essentially indicates physical adsorption. On the other hand, the positive value (+) for Fe_3O_4 infused with the sandstone indicates an endothermic interaction behaviour, where the intramolecular energy is not dissipated but rather stored in the form of newly created chemical bonds. Thus, the interaction can be considered as chemisorption.

3.1.2 Optimization and interfacial strength

Optimization of the models revealed that Fe_3O_4 could induce significant changes in the distribution of oil chains around the sand rock surface. In particular, in the presence of Fe_3O_4 nanoparticles shown in Fig. 5, oil chains are moved or/and bent towards these nanoparticles. The absolute value of sum of the total energies of all isolated components of the systems is bigger than the absolute value of the total energy of the interacting system. In other words, NPs still considerably lowers the interface strength, thus making the removal of oil
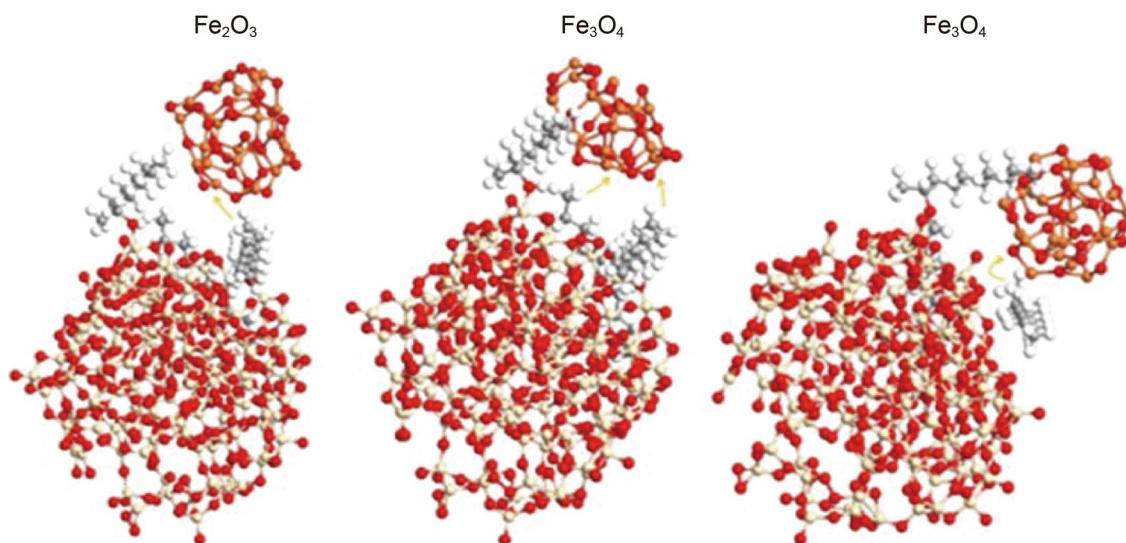
Fig. 5 Visualization of fully optimized basic models in which oil molecules moved or/and bent towards nanostructures. The C, H, O, Si, Fe, atoms are shown in grey, white, red, pink, orange, respectively. Yellow arrows indicate the change of oil chain structure with respect to the reference models

Table 1 Interfacial strengths (γ) of systems containing quartz grains, three oil chains and different types of nanostructures

Grain	Nanostructure	Interfacial strength γ, J/m^2
Quartz	Fe_2O_3 (r_{in} = 5 Å)	0.06797
Quartz	Fe_3O_4 (r_{in} = 5 Å)	0.12538
Quartz	Fe_3O_4 (cluster)	0.06766

(decomposition of the system) energetically preferred. The calculated values of interfacial strength values are given in Table 1. The Fe_3O_4 NPs displayed comparably higher interfacial strength with the sandstone than Fe_2O_3 NPs, as shown in Table 1. However, the interfacial strengths of Fe_3O_4 cluster and Fe_2O_3 NPs are similar, which implies Fe_3O_4 NPs are more effective when stable and well-dispersed in the fluid as compared to when aggregated into clusters.

3.1.3 Stress autocorrelation function (SACF)

This pressure function denotes shearing force. The SACF accounts for the stresses imparted on the system due to the diffusion of molecules and intermolecular kinetics, i.e. molecular stresses caused by attraction and repulsion of molecules. However, as it approaches the stability, the SACF starts to converge to a monotonic level, which satisfies that the viscosity analysed is acceptable. The SACF is a protocol under the Forcite module of the molecular dynamics simulations, which was used to calculate shear stresses of Fe_2O_3 and Fe_3O_4 nanofluids at reservoir temperature of 119 °C and pressure range of 500–25,000 psi. The SACF values of the nanofluids across the pressure range (500–25,000 psi) were plotted, as shown in Fig. 6. Interestingly, the SACF values for Fe_2O_3 show consistently higher values of approximately 0.021 across the pressure range; however, the SACF of Fe_3O_4 nanofluid is stable (0.00128) from pressure values of 0–15,000 psi, then increases to 0.025. These SACF values indicate the Fe_3O_4 NPs are more stable within reservoir pressure conditions (4000–5000 psi) and high temperature with suitable viscosity to improve oil mobility and enhance sweep efficiency.

3.2 Morphological characterization

3.2.1 Adsorption of Fe$_2$O$_3$ and Fe$_3$O$_4$ on quartz

The surface morphologies of the reservoir sandstone aged in the ferrofluids was characterized using FESEM. For Fe_2O_3, NPs interaction with sandstone, platy booklets of kaolinite and distinct polygonal quartz crystal faces were observed (Fig. 7a). The characteristic conchoidal and planar fractures
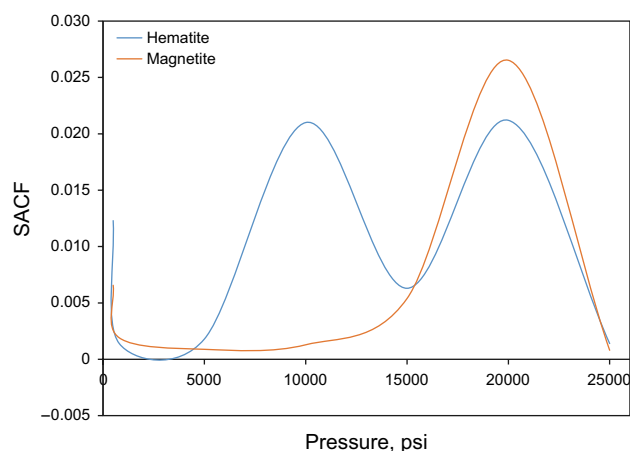
Fig. 6 Plot of SACF values for Fe_2O_3 and Fe_3O_4 nanofluids at different pressures

of quartz are apparent. The Fe_2O_3 NPs are simply deposited on the quartz surface (i.e. physio-sorption) with no clear solid–solid/liquid–solid phase reaction. In contrast, the Fe_3O_4-infused reservoir rocks show free-flowing and undulating surface with globular-shaped terminations (Fig. 7b), and no tendency to form aggregates. The Fe_3O_4 NPs coat the entire quartz surface, making it indiscernible, indicating occlusion or possible chemisorption of the magnetite on the sandstone.

3.2.2 Elemental mapping

Elemental mapping was conducted on the sandstone surface (specifically Fe ions) to corroborate the FESEM micrographs. The Fe elements are sparsely distributed across the surface of Fe_2O_3 imbued with sandstone (Fig. 7c). In contrary, the mapped FESEM image of Fe_3O_4 NPs infused with reservoir sandstone show uniform distribution of Fe element over the sandstone surface (Fig. 7d). This disparity in Fe distribution further suggests the higher adsorption capacity of the Fe_3O_4 nanofluid on the reservoir sandstone compared to Fe_2O_3. This higher dispersibility of Fe_3O_4 supports its ability to infuse with oil and disrupt the wettability of the oil molecules on the rock surface. The images and EDX analysis of the sandstone pore (Fig. 7d) indicate the presence of Fe infused with the oil and matrix material, which infers that the Fe_3O_4 effectively infiltrates the rock and adsorbs on the pore filling matrix material.

3.2.3 EDX composition analysis

The elemental concentrations of the ferro-nanofluids infused with the reservoir sandstone were analysed with EDX (Table 2). Spot analysis was performed for the sandstone grain and matrix (pore infill) material. The absorbed
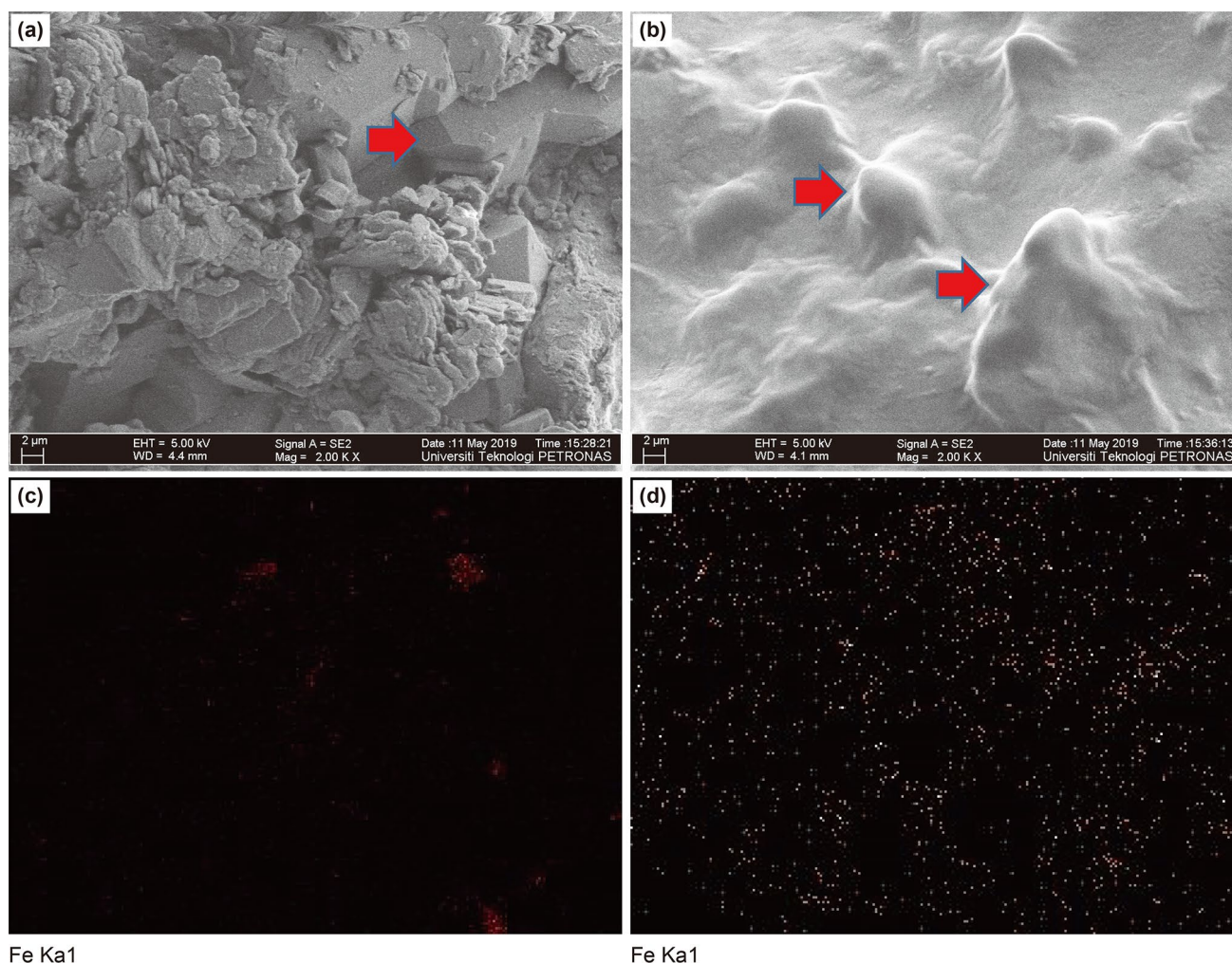
Fig. 7 FESEM micrographs of **a** Fe_2O_3 infused with reservoir sandstone, with inset arrow indicating quartz fracture and **b** Fe_3O_4 infused with reservoir sandstone, with the inset arrow showing quartz terminations are coated. Surface Fe elemental mapping of **c** Fe_2O_3, and **d** Fe_3O_4 infused with reservoir sandstone

Table 2 Elemental distributions [weight percent (wt%) and atomic percent (at%)] of Fe_2O_3 and Fe_3O_4 infused with sandstone, showing higher adsorbed Fe ions and carbon in the case of Fe_3O_4

Sample	S		O		C		Al		Na		Fe		Cl	
	wt%	at%	wt%	at%	wt%	at%	wt%	at%	wt%	at%	wt%	at%	wt%	at%
Fe_2O_3 infused with reservoir sandstone	17.14	9.30	37.21	35.42	42.82	54.30	0.59	0.33	0.22	0.99	1.64	0.45	–	–
	39.58	30.07	43.29	57.73	–	–	1.97	1.56	5.63	5.22	1.34	0.51	7.82	4.70
	11.31	9.43	31.99	45.57	–	–	10.38	8.72	22.28	21.66	1.52	0.49	22.42	14.22
Fe_3O_4 infused with reservoir sandstone	13.83	7.34	6.59	6.14	60.59	76.11	3.14	2.29	8.49	3.43	7.55	2.30	–	–
	15.77	9.01	13.48	11.88	62.77	75.66	–	–	0.95	0.56	6.96	2.12	2.08	0.72
	3.43	1.67	15.55	13.30	71.69	81.64	2.43	1.23	0.38	0.13	6.53	1.99	–	–

Fe ions were found to vary between the infused Fe_2O_3 and Fe_3O_4. The Fe_2O_3 infused with sandstone showed relatively lower adsorbed Fe ions ($\approx 0.5\%$) compared to Fe_3O_4 infused with sandstone ($\approx 2\%$). The amount of adsorbed carbon also varied from 50% for Fe_2O_3 infused sample to 80% for Fe_3O_4 infused sample. This implies that the concentration

of available C atoms from the oil retained in the reservoir system increases with adsorbed Fe.

3.3 FTIR analysis

The FTIR spectra of the various sandstones aged under different conditions (brine, brine+crude, brine+crude+nanofluids) are shown in Figs. 8, 9 and 10. The functional groups (band assignments) detected by FTIR spectroscopy of the sandstone samples are given in Table 3. The functional groups detected in the FTIR spectra of the various samples are presented and their variations are determined in the underlying subsections.

3.3.1 Silicate and H–O–H bonds

The FTIR spectra of the sandstone samples show the characteristic peaks for siloxane (Si–O–Si), Si–O quartz, Si–O stretching and bending vibrations (Fig. 8). After ageing with crude oil, brine, and Fe_2O_3 and Fe_3O_4 nanofluid solutions, the characteristic peaks of Si–O symmetrical stretching, Si–O symmetrical bending and Si–O asymmetrical stretching vibrations within the ranges of 694, 777–797 and 1083–1099 cm^{-1}, respectively, remain for all samples (Fig. 8). However, the absorbance peaks for Si–O–Si bending at 644 cm^{-1} and H–O–H bending of water 1640 cm^{-1}

in the spectra of sandstone aged in brine, but absent in samples infused with oil, indicate the masking of the siloxane bond and displacement of water by crude oil. The distinct absorption bands at 1030 cm^{-1} and 1006 cm^{-1} are ascribed to framework Si–O–Si stretching vibrations. The absorption bands at 935 cm^{-1} and 910 cm^{-1} represent the Al–OH bending vibrations. The band at 935 cm^{-1} is also attributed to the non-bonding of inner surface or surface (nanostructure) OH. The reduction in the cusp of the characteristic peak of H–O–H bonding in the spectrum for sandstone immersed in brine can be attributed to the ability of Fe_2O_3 and Fe_3O_4 fluids to accelerate oil removal in water–oil emulsion (Ko et al. 2014). The observed shift in the siloxane (Si–O–Si) and Si–O quartz bonds indicate adsorption of Fe–O from magnetite to SiO_2.

Higher-resolution FTIR spectra were obtained for low-wave number region (1300–650 cm^{-1}) to clearly show the variations in the functional groups (Fig. 9). The characteristic absorption bands for Fe hydr(oxides) were identifiable within the spectral range of 170 cm^{-1} and 570 cm^{-1}, which were beyond the detection limit of instrument used in this study. Absorption bond was identified at 750 cm^{-1} in FTIR spectra of Fe_3O_4 infused in the sandstone, which is assigned to out of plane FeOOH vibrations. Nonetheless, the Fe–O band indicates the presence of maghemite, a defective form of magnetite. The presence of FeOOH and Fe–O
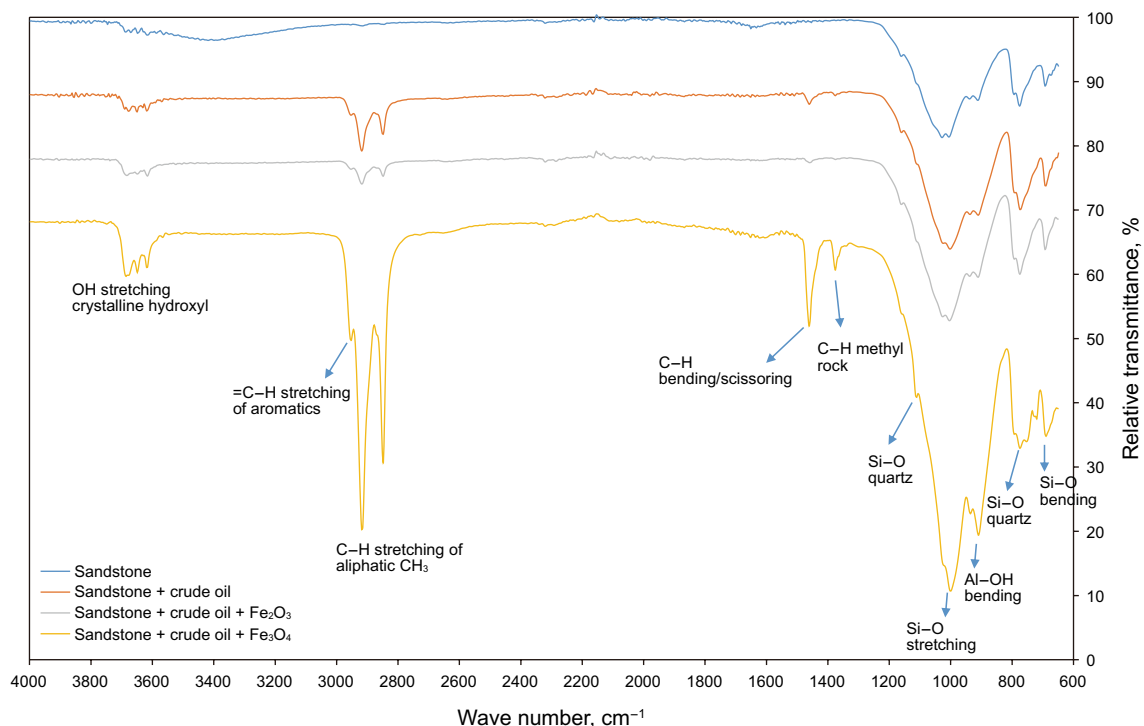
Fig. 8 Stacked FTIR spectra of sandstone, sandstone aged in crude oil, sandstone aged in crude oil and Fe_2O_3 nanofluid, and sandstone aged in crude oil and Fe_3O_4 nanofluid
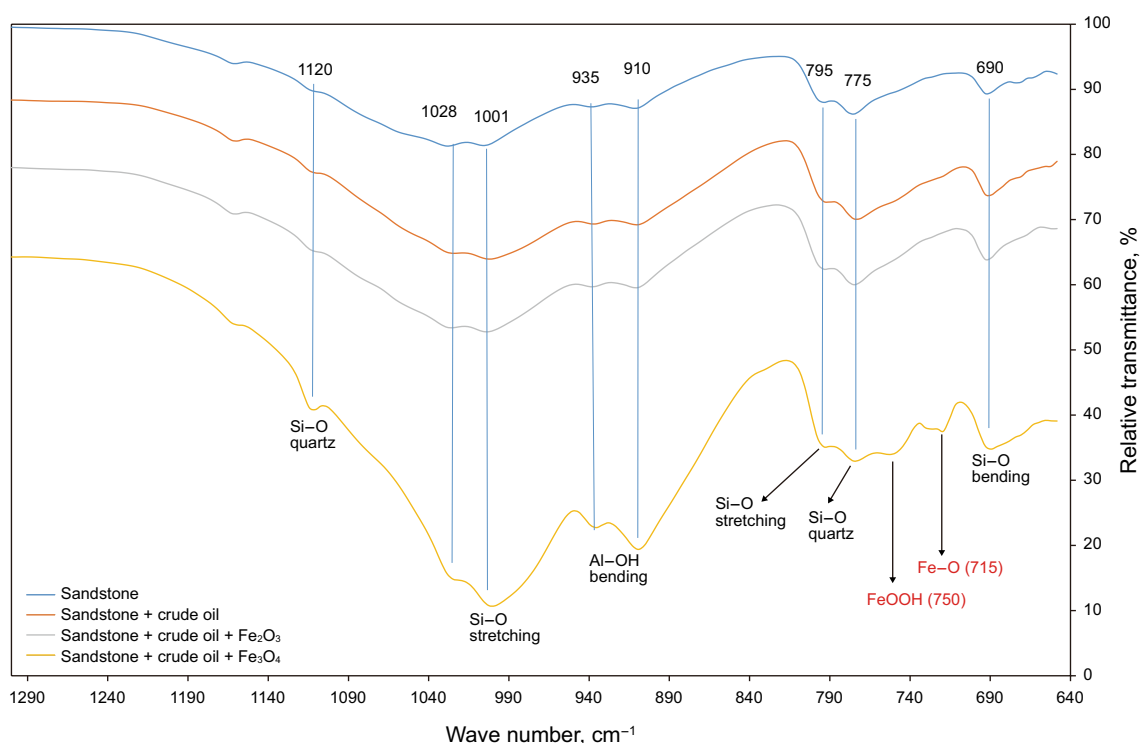
Fig. 9 Closer view of the low-wave FTIR region (600–1300 cm^{-1}) for sandstone, sandstone aged in crude oil, sandstone aged in crude oil and Fe$_2$O$_3$ nanofluid, and sandstone aged in crude oil and Fe$_3$O$_4$ nanofluid
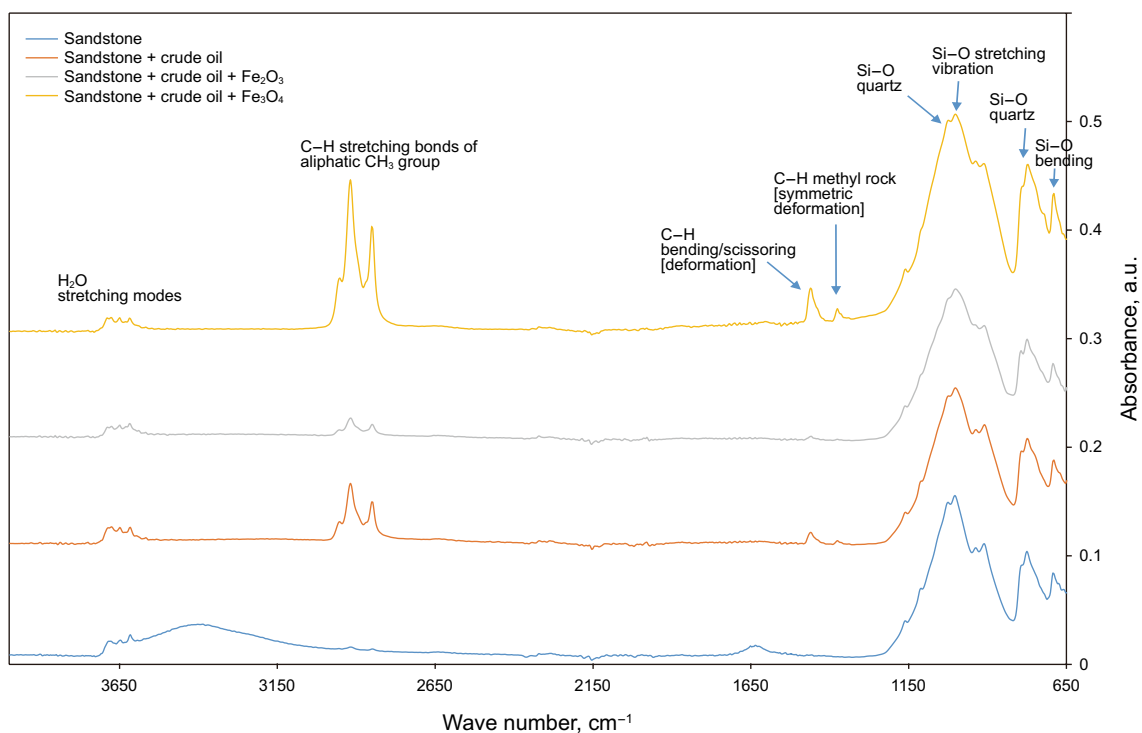
Fig. 10 Overlapping FTIR absorbance spectra of sandstone, sandstone aged in crude oil, sandstone aged in crude oil and Fe$_2$O$_3$ nanofluid, and sandstone aged in crude oil and Fe$_3$O$_4$ nanofluid

Table 3 Functional groups (band assignments) detected by FTIR spectroscopy of the sandstone samples

Wave number, cm^{-1}				Type of vibration
Sandstone	Sandstone+crude oil+brine	Sandstone+crude oil+brine+Fe$_2$O$_3$ (hematite)	Sandstone+oil+brine+Fe$_3$O$_4$ (magnetite)	
3640	3640	3640	3640	Al–O–H stretching, OH stretching, crystalline hydroxyl
3418	–	–	–	Stretching modes of surface H$_2$O molecules or envelope of hydrogen-bonded (absorbed) surface OH groups
2916	2918	2917	2917	Asymmetric and symmetric stretching vibrations of C–H bonds of aliphatic CH$_3$ group
–	2849	2849	2849	Asymmetric and symmetric stretching vibrations of C–H bonds of aliphatic CH$_3$ group
1644	–	–	–	H–O–H bending of water
–	1461	1459	1461	C–H deformation (bending vibration of C–H of CH$_2$ and CH$_3$ aliphatic groups)
1388	1389	1388	1389	Al–O as Si cage
–	1375	1375	1376	C–H symmetric deformation
1028	1028	1030	1028	Si–O asymmetrical stretching vibration; clay minerals
1001	1001	1004	1001	Si–O stretching vibrations
1084	1082	1085	1084	Si–O quartz
935	935	936	936	Non-bonding inner surface or surface (nanostructure) OH; Al–OH deformation vibration
912	912	911	910	Al–OH bending vibration; Al–OH bending vibrations (deformation linked to 2Al^{3+}); Al–OH stretching vibrations for aluminium in octahedral position (kaolinite)
795	796	795	795	Si–O symmetrical stretching vibration
776	776	775	774	Si–O quartz; hydroxyl group (Al–OH) perpendicular to the surface (Translational –OH)
–	–	–	735, 695	Substituted aromatics C-H bonds of benzene ring
692	691	691	689	Si–O symmetrical bending vibrations
644	–	–	–	Si–O–Si bending

bands affirms the existence of both ferrous (Fe^{2+}) and ferric (Fe^{3+}) ions, which implies the stability of the Fe$_3$O$_4$ within an environment where oxidative and reductive states of Fe occur and are sustained.

3.3.2 C–H bonds

Two intense C–H stretching vibrations were also identified at around 2920 cm^{-1} and 2850 cm^{-1}, for sandstone samples saturated with crude oil, brine, and nanofluid solution. The C–H stretching bands in 2850–2958 cm^{-1} are indicative of polyatomic C$_n$–H–O entities with C bonded to two or three H. The highest intensity (y_{CH}) band between 2920 and 2931 cm^{-1} is assigned to symmetrical stretching of C–H mode of –CH$_2$-group. A spectral peak is also discernible at 1460 cm^{-1}, which is assigned to C–H deformation of the saturate due to vibration of the carboxylic acid group present in the crude. C–H symmetric deformation of the saturate (1376 cm^{-1}) was also detected, although with larger intensity in the sample aged in the Fe$_3$O$_4$ nanofluid. This

relatively higher intensity is suggestive of the displacement of oil by the Fe$_3$O$_4$ nanofluid, thus enabling improved detection of the C–H peak. In addition, the presence of a peak denoting substituted aromatics C–H bonds of benzene ring at 715 cm^{-1} (Fig. 8), which is conspicuously absent in the spectra of other samples. This band is assigned to long-chain methyl rock. Stacked FTIR spectra show variations in peaks and band intensities. The FTIR spectrum for sandstone samples treated with crude oil and Fe$_3$O$_4$ shows the highest peak intensities for characteristic C–H bond stretching (symmetric and asymmetric) vibration. Overlapping FTIR spectra show characteristic C–H bond stretching (symmetric and asymmetric) vibration for sandstone samples treated with crude oil, and Fe$_3$O$_4$ nanofluid have the highest peak compared to the other samples. The saturate fraction has dominant aliphatic hydrocarbons (alkanes) as indicated by the complete presence of absorbance near 2920, 2850 and 1450 cm^{-1} and the absence of absorption near 1600 cm^{-1}, which is the characteristic band for aromaticity. Although the presence of the absorption band at 715 cm^{-1} in the spectra of Fe$_3$O$_4$ infused

with the sandstone sample is proof of the aromaticity, the C–H stretch band at 3000–2850 cm^{-1} is the most intense because the change in dipole moment with respect to distance for the C–H stretching is greater compared to others. The weak bond at 3083 cm^{-1} is assigned to =C–H stretching, which indicates the presence of alkenes and aromatics.

The Fe_3O_4 infused sandstone sample shows the highest absorbance for the Si–O quartz, Si–O–Si and C–H bonds (Fig. 10). The higher intensity for Fe_3O_4-infused sandstone sample is attributed to greater change in dipole moment with respect to distance. The peak shifts and higher adsorbance intensities in the case of Fe_3O_4-infused sandstone sample imply disturbance of the adsorption layers of oil molecules existing on the solid surface by FeOOH and Fe–O compounds, which contributes to the detached oil molecules. The cusp observed for the pure sandstone, which is absent in the other spectra, denotes stretching modes of surface H_2O molecules. This absence suggests the possible expulsion of connate and adsorbed water molecules with the introduction of the NPs.

3.4 X-ray photon spectroscopy

The powder samples were also studied with XPS to comprehensively analyse the implications of their oxidative phase, which determines the properties of iron oxide NPs. The XPS method subjects the samples to EM irradiation from a soft X-ray source under ultrahigh vacuum, which results in the absorption of the EM by the electrons contained in the samples (with binding energy less than the vacuum level). The absorbed EM radiation is subsequently dispelled from the solid with a kinetic energy that is then analysed. The scattered electrons have an energy that is typical of the element from which they are emitted, and the intensity of the characteristic peaks observed in the energy spectra is related to the concentration of the elements present in the surface through relative sensitivity factors proper of each instrument. The relative intensities of the oxide and elemental peaks change with the oxide thickness.

XPS spectra were obtained for different samples (Fig. 11). The spectra reveal the existence of carbon, sodium (Na 1s, 1071–1071.5 eV: derived from the brine used to disperse the nanoparticles), oxygen (1s, 532.2 eV), two forms of carbon: carbon singly bonded to an oxygen atom (1s, 286.5 eV, and carbon singly bonded to a hydrogen atom as in aliphatic chains (1s, 284.6 eV), two forms of silicon: silicon singly bonded to an oxygen atom (2p, 103.5 eV) and silicon bonded to a C–H chain (2p, 102.5 eV), aluminium (2p, 74.5 eV) and Fe (accessory minerals in the Berea sandstone). Some samples also exhibit chlorine (2p, 198.5 eV). The reference line for all the XPS spectra was organic carbon (1s, 284.6 eV). Adventitious carbon content is negligible. The strong intensity peak of C suggests organic/biogenic source or catalytic

interaction of C- and H-containing compounds and the quartz surface, rather than from mere exposure to air. The C centred at 285 eV denotes organic species with C–H, C–C and C–O bonds (Hochella 1988; Hochella et al. 1990). The existence of the oxygenated carbon may possibly augment the hydrophilic character of the ferrofluids. However, the characteristic XPS peaks for Si, C and Fe are absent in the spectral of sandstone samples aged in magnetite, suggesting the intense adsorption of the magnetite with the crude oil. Underlying subsections provide detailed explanation of the XPS survey spectra for silicon and carbon. The XPS parameters are given in Table 4.

3.4.1 XPS silicon spectra

The chemical state of Si in these XPS spectra is SiO_2 (quartz), as indicated by the binding energies at ≈ 104 eV. The spectral variation of the different samples with regard to Si is shown in Fig. 12. For pure sandstone (Fig. 12a), the identified peaks include Si 2p (oxide) and Si 2p (element) at 104 eV and ≈ 99 eV, respectively. With the addition of crude oil and Fe_2O_3, Si 2p (oxide) peak becomes symmetric at binding energy of ≈ 104 eV (Fig. 12b, c). For Fe_3O_4, the characteristic peak for Si 2p (oxide) diminishes. This distorted binding energy spectrum for Fe_3O_4-infused sample (Fig. 12d) suggests high adsorption and interfacial energy between Si and Fe_3O_4, which led to the poor resolution of spin–orbit components.

3.4.2 XPS carbon spectra

For the bare sandstone sample (Fig. 13a), the carbon identified at binding energy of ≈ 285.7 eV denotes adventitious carbon (C–O–C), which is likely derived from exposure of the sample to the atmosphere. Also observed is a C 1s component at the left, indicating the presence of ester (O–C=O), which similarly points to adventitious carbon. For the sample aged with crude oil and brine, the carbon peak is identified at energy position of 286 eV with high counts/s of $> 17,000$ (Fig. 13b, c). Based on its symmetry, this C 1s peak is denoted as phenyl. Extended delocalized electrons in the sample (e.g. aromatic rings) can result in a satellite structure, several eV to higher binding energy of the main peak, as in the case of Fe_3O_4-infused oil (Fig. 13d).

3.5 Interfacial tension (IFT)

The interfacial tensions between crude oil and nanometric colloidal Fe_2O_3 and Fe_3O_4 dispersed in brine were investigated. The measured IFT for brine/oil, Fe_2O_3/oil and Fe_3O_4/oil are 40, 36.17, and 35 mN/m, respectively. Figure 14 shows the distribution of IFT values with time for different nanofluids and brine as control sample. The IFT
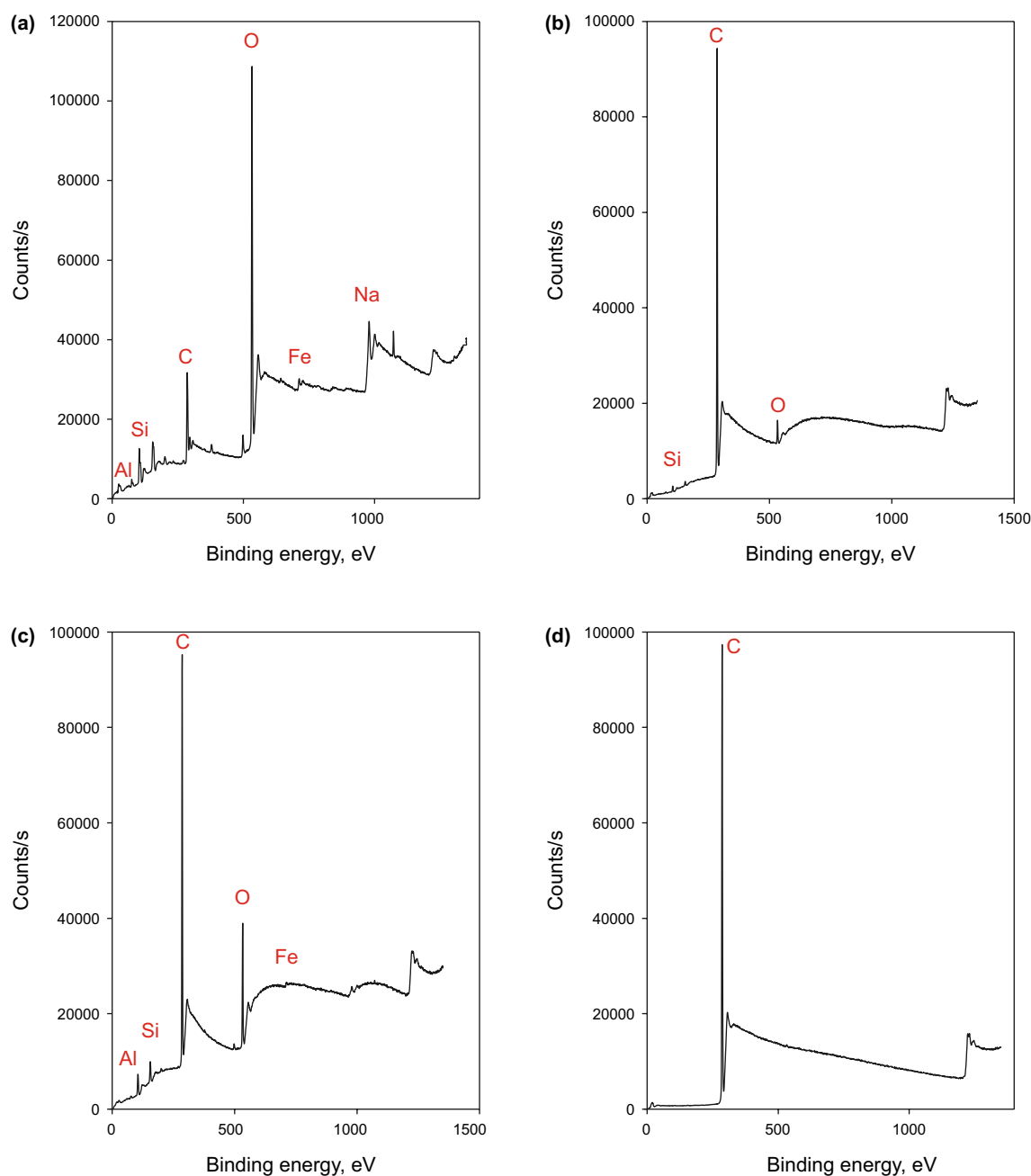
Fig. 11 XPS survey spectra of **a** sandstone, **b** sandstone aged in crude oil, **c** sandstone aged in crude oil and Fe$_2$O$_3$ nanofluid, **d** sandstone aged in crude oil and Fe$_3$O$_4$ nanofluid

properties are dependent on the particle attachment at the interface. The variation in IFT is as a result of the hydrophilic or lipophilic character of the particles, which is the basis of their affinity for the fluid interface. For the Fe$_2$O$_3$ nanofluid infused with crude oil, the utilized particles are strongly hydrophilic, which are then completely wetted and do not influence the properties of the aqueous dispersion interface. Instead, the surfaces of Fe$_3$O$_4$ nanoparticles have a higher hydrophobicity and adsorption, providing a

driving force for their attachment at the biphasic liquid/fluid interface (Felicia et al. 2016). Thus, Fe$_3$O$_4$ reduced IFT by as much as approximately 14.3%, whereas Fe$_2$O$_3$ showed a slightly lower reduction of 3.3% on the average. The reduced IFT can be attributed to the electrostatic repulsive interactions between the Fe$_3$O$_4$ NPs and the oil surface, which promotes the diffusion of the nanoparticle towards the interface (Ma et al. 2008). The nanoparticle adsorption strongly influences the hydrophobicity/

Table 4 XPS parameters for Fe_2O_3 and Fe_3O_4 infused with reservoir sandstone

Sample	Si 2p bend-ing energy, eV	Si 2p counts/s	C 1s bend-ing energy, eV	C 1s counts/s	Fe 2p_{3/2} bend-ing energy, eV	Fe 2p_{3/2} counts/s	Fe 2p_{1/2} bend-ing energy, eV	Fe 2p_{1/2} counts/s
Sandstone	104	1100	285.7	5372	713	30,218.5	724	29,589
	107	1700						
Sand-stone + crude oil (Fig. 13b)	105	400	286	16,983	712	17,150	724	17,106
Sand-stone + crude oil + Fe_2O_3 (Fig. 13c)	103	1400	285.5	17,096	710	26,446	723	26,378
Sand-stone + crude oil + Fe_3O_4 (Fig. 13d)	103.5	79	285.6	16,380	709	11,464	725	11,262

lipophilicity of the particle, i.e. the particle affinity for the fluid interfacial environment (Levine et al. 1989). The Brownian transport of particles from the bulk to the interface, argued on the basis of the relaxation of dynamic interfacial tension after large expansions of the interfacial area, is most likely ineffective here. In fact, for energetic reasons, the attachment of the particles at the fluid interface is essentially an irreversible process. Moreover, the strongly magnetoresponsive character of Fe_3O_4 accounts for its high adsorption energy (Socoliuc and Vékás 2014).

3.6 Magnetization measurements

The magnetic properties of the Fe_2O_3 and Fe_3O_4 NPs were also studied using VSM. The hysteresis loops of Fe_2O_3 and Fe_3O_4 NPs at room temperature are shown in Fig. 15. The magnetization study conducted as a function of magnetic field shows hysteric behaviour with coercivity (G) of 123.61 and 96.24 for Fe_2O_3 and Fe_3O_4, respectively. The remanent magnetization (retentivity) values are 3.56 and 4.013 emu/g, and the saturation magnetization values are 32.25 and 40.97 emu/g for Fe_2O_3 and Fe_3O_4, respectively (Table 5). The higher saturation magnetization and retentivity for Fe_3O_4 can be ascribed to its greater interparticle magnetic interaction. However, the value obtained for magnetite in this study is much smaller than 91.5 emu/g reported for nanocrystalline magnetite (Ozdemir et al. 2002), and 98 emu/g recorded for bulk magnetite (Cullity 1972). That significant incongruity can be attributed to a possible nonparallel coupling of the magnetization in the surface regions of grains or the presence of impurities that might have appeared during synthesis (Starowicz et al.

2011). The nanoparticle size could also account for this relatively low magnetization.

4 Discussion

Given the dearth of knowledge on the application of ferrofluids in EOR, this study investigated the interaction of Fe_2O_3 and Fe_3O_4 NPs with sandstone. The kinetics of sorption seems to be faster for Fe_3O_4 than for Fe_2O_3. Based on its high adsorption to the reservoir sandstone and ability to infill pore spaces, the effect of Fe_3O_4 on hydrocarbon recovery is twofold. The Fe_3O_4 can either increase the viscosity of the displacing fluid, resulting in a higher sweep efficiency or infuse (soaked) with the oil, which can then be attracted and recovered through the application of inward magnetic forces towards the borehole. The SACF value of Fe_3O_4 corroborates this ability to accelerate oil removal in a water-in-oil emulsion. Thickening of the Fe_3O_4 infused with crude oil occurs due to ability of the NPs to form a network structure via hydrogen bonding (Zeyghami et al. 2014), which will directly affect the fluid shear stress (Cheraghian and Hendraningrat 2016). On the other hand, the negative charges on the FeOOH surface of Fe_2O_3 are higher, which accounts for the less favourable adsorption. The results show that silica and clays exhibit a high affinity to surfaces of Fe_3O_4, as confirmed by the significant increase in absorbance spectral intensity. It is therefore reasonable to suggest that the increase in intensity is due to the sorption of low polymeric silicate species and possibly the enhanced polymerization at the Fe_3O_4 surface. Thus, the strong infrared absorbance in the wavenumber region 1050–1200 cm^{-1} is related to the polymeric species, while the appearance of the band at about 1120 cm^{-1} could be an infrared spectral evidence for the
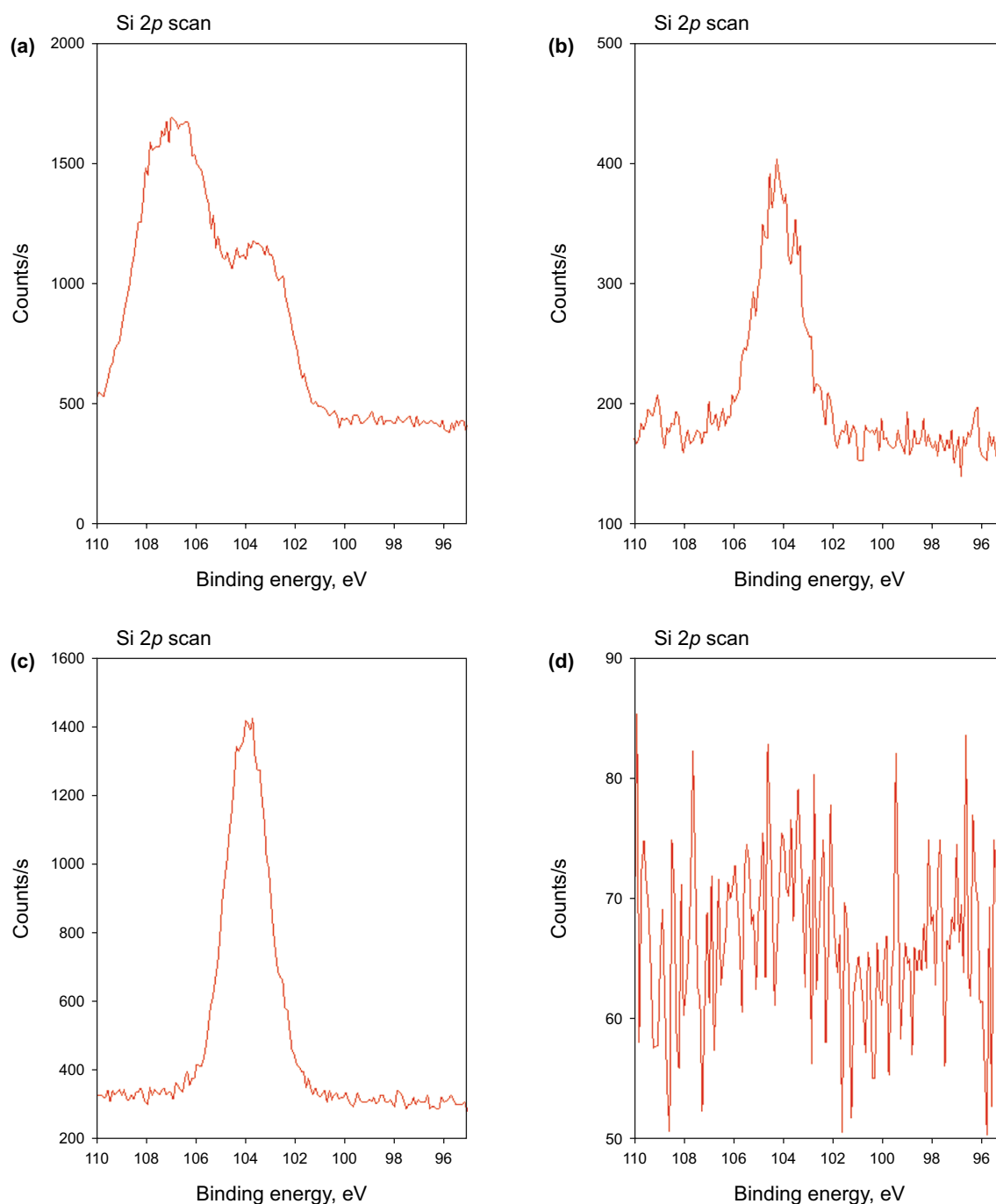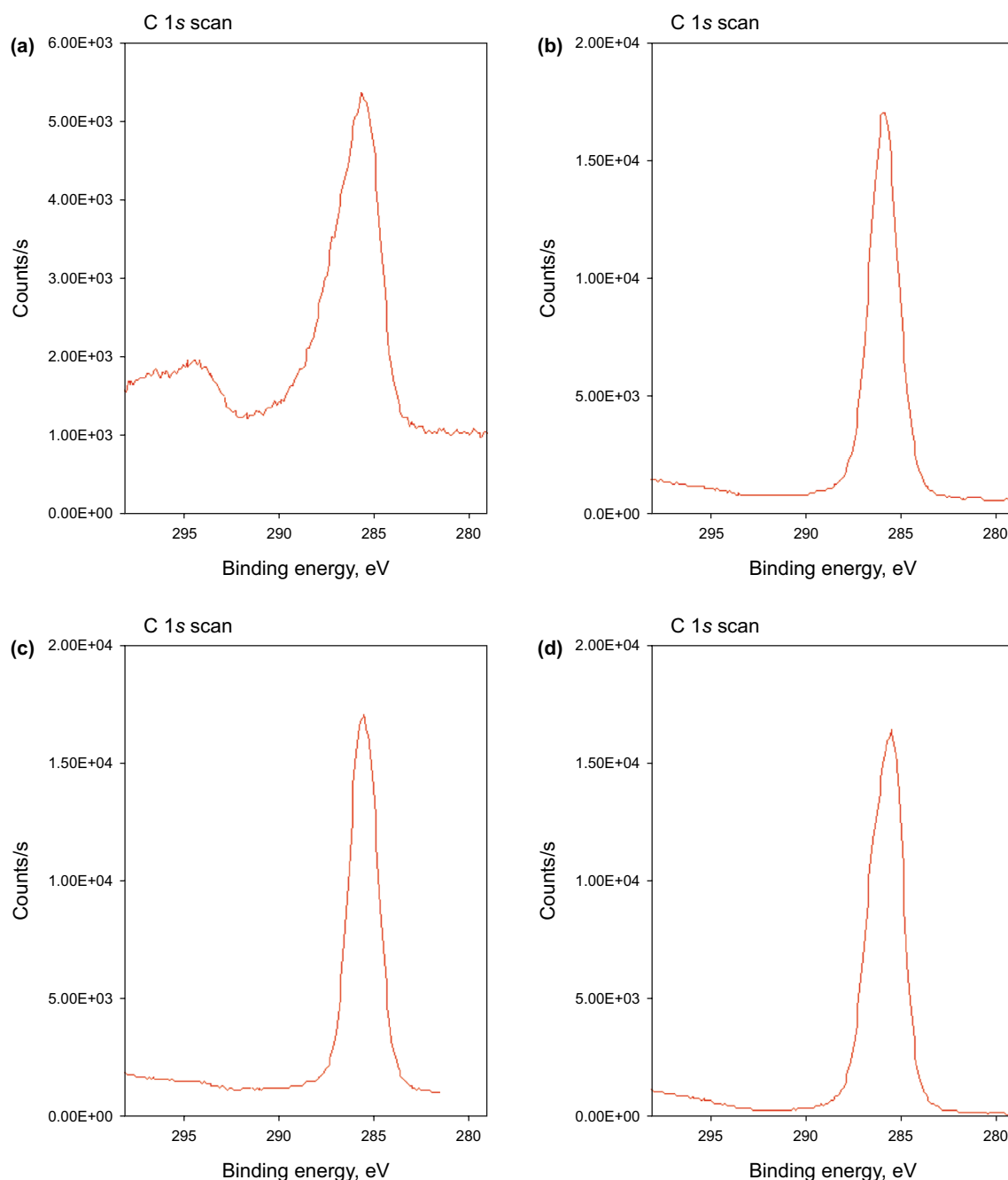
Fig. 12 High-resolution XPS spectra of silicon (Si 2p) for **a** sandstone, **b** sandstone aged in crude oil, **c** sandstone aged in crude oil and Fe_2O_3 nanofluid, and **d** sandstone aged in crude oil and Fe_3O_4 nanofluid

formation of a 3D framework silica structure on the Fe_3O_4 surface.

The simulated and measured parameters for Fe_2O_3 and Fe_3O_4 ferrofluids are given in Table 6. Fe_2O_3 and Fe_3O_4 ferrofluids were shown experimentally to reduce IFT, with Fe_3O_4 ferrofluid presenting a higher decrease. By decreasing the IFT and altering the rock wettability using ferrofluids,

the capillary pressure will decline, resulting in improved oil recovery (Roustaei et al. 2012). In the case of Fe_2O_3, the self-organization of dipolar Fe_2O_3 cubes into dipolar chain morphology accounts for its effect on IFT. Fe_3O_4 NPs apparently improved the rheology of the dispersing brine solution as it adsorbed to the fluid. The Brownian motion of the Fe_3O_4 NPs in the bulk and the internal restructuring of the

Fig. 13 High-resolution XPS spectra of carbon (C 1*s*) for **a** sandstone, **b** sandstone aged in crude oil, **c** sandstone aged in crude oil and Fe$_2$O$_3$ nanofluid, and **d** sandstone aged in crude oil and Fe$_3$O$_4$ nanofluid

mixed particle (brine-Fe$_3$O$_4$-oil) layer at the interface and the Fe$_3$O$_4$ rearrangement between the attached nanoparticles and the fluid interface (nanofluid solution/hexane interface) account for the IFT reduction (Ravera et al. 2006).

The high adsorption property of Fe$_3$O$_4$ also supports its potential use as a removal agent of microscopic oil droplets and remnant polymer from produced water, as well as divalent cations (Ca^{2+}) from hard brine. The catalytic properties of Fe$_3$O$_4$ NPs can potentially enable

in situ cracking of oil chains, significantly improving the efficiency of EOR. Thus, the magnetite normally exerts effects on oil degradation by modifying the concentrations of the free radicals. This study is consistent with the previous studies. Shekhawat et al. (2016) proposed the application of Fe$_3$O$_4$ nanofluids for magnetic heavy oil recovery. The differential impact of the ferro-nanofluids is compelled by competing anisotropic interactions caused by the variable particles' shapes [spherical (Fe$_3$O$_4$) and
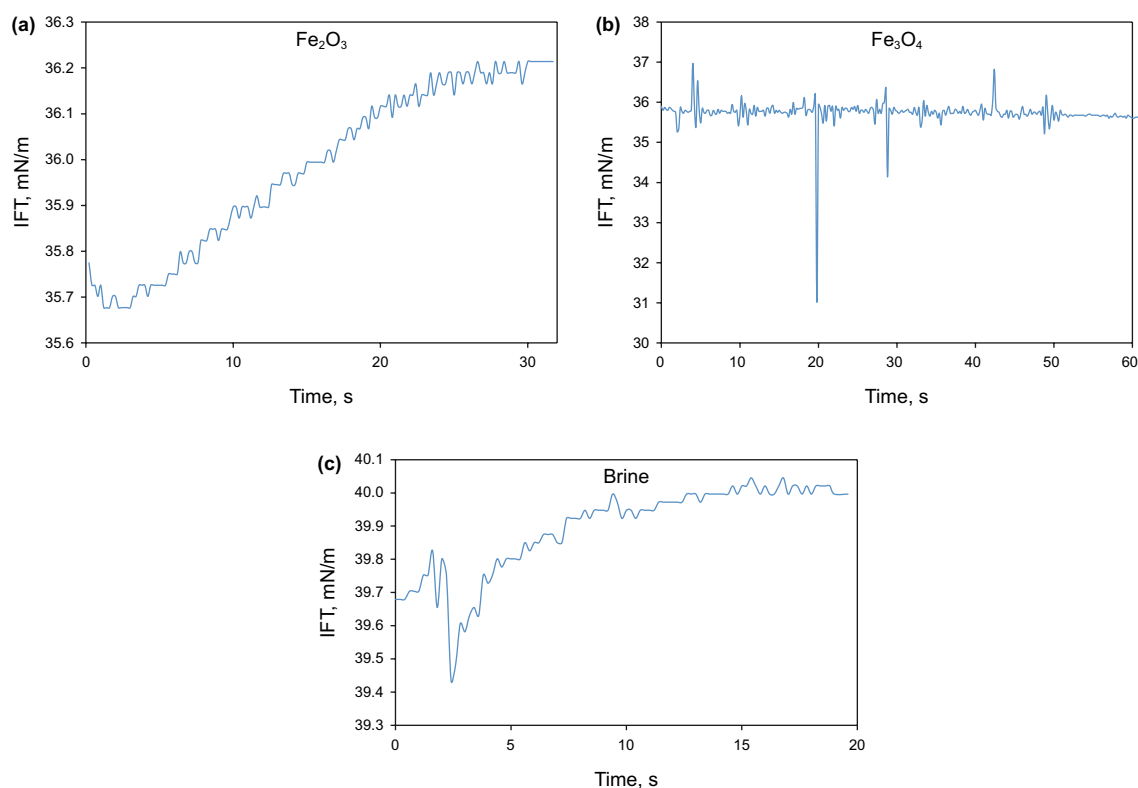
Fig. 14 IFT of **a** crude oil and Fe$_2$O$_3$ nanofluid, **b** crude oil and Fe$_3$O$_4$ nanofluid, **c** brine and oil
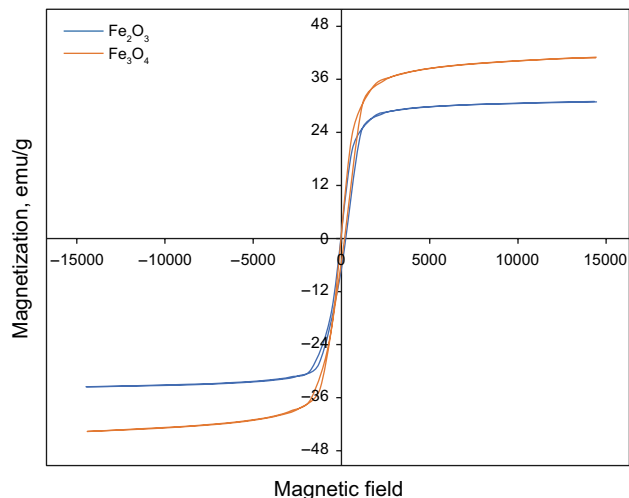
Fig. 15 VSM magnetization curves of Fe$_2$O$_3$ and Fe$_3$O$_4$

Table 5 Summary of Fe$_2$O$_3$ and Fe$_3$O$_4$ magnetic properties

Sample	Saturation magnetization, emu/g	Coercivity G	Retentivity, emu/g
Fe$_2$O$_3$	32.25	123.61	3.56
Fe$_3$O$_4$	40.97	96.24	4.013

cubical (Fe$_2$O$_3$)] and their dipole moments (Rossi et al. 2018). As indicated by their saturation magnetization and retentivity (remanent magnetization), the Fe$_3$O$_4$ displays higher interparticle magnetic interactions, which enables interaction between the oil and Fe$_3$O$_4$.

5 Conclusion

In situ ATR-FTIR and XPS spectroscopies were used to monitor the sorption of ferro-nanoparticles (Fe$_2$O$_3$ and Fe$_3$O$_4$) on silicates. The observed spectral changes indicate Fe$_3$O$_4$ infused with the reservoir sandstone has a higher silicate adsorption capacity than Fe$_2$O$_3$, possibly because of their larger number of active surface sites and the existence of both ferrous (Fe^{2+}) and ferric (Fe^{3+}) ions, which implies the stability of the magnetite within an environment where oxidative and reductive states of Fe are present. The Fe$_3$O$_4$ nanofluid exhibits a higher IFT reduction, which can be attributed to its strongly magnetoresponsive characteristics, higher hydrophobicity and adsorption, providing a driving force for their attachment at the biphasic liquid/fluid interface.

Table 6 Values of simulated and measured parameters for Fe_2O_3 and Fe_3O_4 infused with reservoir sandstone

Simulated and measured parameters	Fe_2O_3 infused with reservoir sandstone	Fe_3O_4 infused with reservoir sandstone
Adsorption, kcal/mol	-2300	100
SACF	0.021	0.00128
Interfacial strength γ, J/m^2	0.06797	0.12538
Interfacial tension, mN/m	36.17	35
Adsorbed Fe ions, %	0.5	2

References

Agista MN, Guo K, Yu Z. A state-of-the-art review of nanoparticles application in petroleum with a focus on enhanced oil recovery. Appl Sci. 2018;8(6):871–99. https://doi.org/10.3390/app8060871.

Allen MP, Tildesley DJ. Computer simulation of liquids. Oxford: Clarendon Press; 1996. p. 385.

Buckley JS, Liu Y. Some mechanisms of crude oil-brine-solid interactions. J Pet Sci Eng. 1998;20:155–60. https://doi.org/10.1016/S0920-4105(98)00015-1.

Cheraghian G, Hendraningrat L. A review on applications of nanotechnology in the enhanced oil recovery part B: effects of nanoparticles on flooding. Int Nano Lett. 2016;6:1–10. https://doi.org/10.1007/s40089-015-0170-7.

Cullity BD. Introduction to magnetic materials. Reading: Addison-Wesley; 1972. p. 491–555.

Dunphy Guzman KA, Finnegan MP, Banfield JF. Influence of surface potential on aggregation and transport of titania nanoparticles. Environ Sci Technol. 2006;40:7688–93. https://doi.org/10.1021/es060847g.

Felicia LJ, Vinod S, Philip J. Recent advances in magnetorheology of ferrofluids (magnetic nanofluids)—a critical review. J Nanofluids. 2016;5:1–22. https://doi.org/10.1166/jon.2016.1203.

Haroun MR, Alhassan S, Ansari AA, Al Kindy NAM, Abou Sayed, N, Kareem A, et al. Smart nano-EOR process for Abu Dhabi carbonate reservoirs. In: Abu Dhabi international petroleum conference and exhibition, 11–14 Nov, Abu Dhabi, UAE; 2012. https://doi.org/10.2118/162386-MS.

Hendraningrat L, Li S, Torsaeter O. A coreflood investigation of nanofluid enhanced oil recovery. J Pet Sci Eng. 2013;111:128–38. https://doi.org/10.1016/J.Petrol.2013.07.003.

Hochella MF Jr. Auger electron and X-ray photoelectron spectroscopies. In: Hawthorne FC, editor. Spectroscopic methods in mineralogy and geology. Reviews in mineralogy, vol. 18. Washington: Mineralogical Society of America; 1988. p. 573–638.

Hochella MF Jr, Eggleston CM, Elings VB, Thompson MS. Atomic structure and morphology of the albite (010) surface: an atomic-force microscope and electron diffraction study. Am Miner. 1990;75:723–30.

Huh C, Nizamidin N, Pope GA, Milner TE, Wang B. Hydrophobic paramagnetic nanoparticles as intelligent crude oil tracers. U.S. Patent application 14/765,426[P]. 2015-12-31.

Joonaki E, Ghanaatian S. The application of nanofluids for enhanced oil recovery: effects on interfacial tension and coreflooding process. Pet Sci Technol. 2014;32:2599–607. https://doi.org/10.1080/10916466.2013.855228.

Kamal MS, Adewunmi AA, Sultan A, Al-Hamad MF, Mehmood U. Recent advances in nanoparticles enhanced oil recovery: rheology, interfacial tension, oil recovery, and wettability alteration. J Nanomater. 2017. https://doi.org/10.1155/2017/2473175.

Khaled KF. Corrosion inhibition by L-arginine Ce^{4+} system: Monte Carlo simulation study. J Chem Acta. 2012;1:59–65.

Ko S, Prigiobbe V, Huh C, Bryant SL, Bennetzen MV, Mogensen K. Accelerated oil droplet separation from produced water using magnetic nanoparticles. In: SPE annual technical conference and exhibition, Amsterdam, The Netherlands, 27–29 Oct 2014; 2014. https://doi.org/10.2118/170828-MS.

Kothari N, Raina B, Chandak KB, Iyer V, Mahajan, HP. Application of ferrofluids for enhanced surfactant flooding in IOR. In: SPE EUROPEC/EAGE annual conference and exhibition. Society of Petroleum Engineers, Barcelona, Spain; 2010. https://doi.org/10.2118/131272-MS.

Levine S, Bowen BD, Partridge SJ. Stabilization of emulsions by fine particles I. Partitioning of particles between continuous phase and oil/water interface. Colloids Surf. 1989;38:325. https://doi.org/10.1016/0166-6622(89)80271-9.

Li S, Hendraningrat L, Torsaeter O. Improved oil recovery by hydrophilic silica nanoparticles suspension: 2 phase flow experimental studies. In: International petroleum technology conference, 26–28 Mar, Beijing, China; 2013. https://doi.org/10.2523/IPTC-16707-MS.

Ma H, Luo M, Dai LL. Influences of surfactant and nanoparticle assembly on effective interfacial tensions. Phys Chem Chem Phys. 2008;10(16):2207–13. https://doi.org/10.1039/b718427c.

Negin C, Ali S, Xie Q. Application of nanotechnology for enhancing oil recovery—a review. Petroleum. 2016;2:324–33. https://doi.org/10.1016/j.petlm.2016.10.002.

Ogolo N, Olafuyi O, Onyekonwu M. Enhanced oil recovery using nanoparticles. In: SPE Saudi Arabia section technical symposium and exhibition, 8–11 Apr, Al-Khobar, Saudi Arabia; 2012. https://doi.org/10.2118/160847-MS.

Ozdemir O, Dunlop DJ, Moskowitz BM. Changes in remanence, coercivity and domain state at low temperatures in magnetite. Earth Planet Sci Lett. 2002;194:343–58. https://doi.org/10.1016/S0012-821X(01)00562-3.

Parvazdavani M, Masihi M, Ghazanfari MH. Monitoring the influence of dispersed nano-particles on oil–water relative permeability hysteresis. J Petrol Sci Eng. 2014;124:222–31. https://doi.org/10.1016/j.petrol.2014.10.005.

Ravera F, Santini E, Loglio G, Ferrari M, Liggieri L. Effect of nano-particles on the interfacial properties of liquid/liquid and liquid/air surface layers. J Phys Chem B. 2006;110:19543–51. https://doi.org/10.1021/jp0636468.

Rezaei Gomari KA, Denoyel R, Hamouda AA. Wettability of calcite and mica modified by different long-chain fatty acids (C18 acids). J Colloid Interface Sci. 2006;297:470–9. https://doi.org/10.1016/j.jcis.2005.11.036.

Rossi L, Donaldson JG, Meijer J, Petukhov AV, Kleckner D, Kantorovich SS, et al. Self-organization in dipolar cube fluids constrained by competing anisotropies. Soft Matter. 2018;14:1080. https://doi.org/10.1039/c7sm02174g.

Roustaei A, Moghadasi J, Bagherzadeh H, Shahrabadi A. An experimental investigation of polysilicon nanoparticles' recovery efficiencies through changes in interfacial tension and wettability alteration. In: SPE international oilfield nanotechnology conference and exhibition, 12–14 June, Noordwijk, The Netherlands; 2012. https://doi.org/10.2118/156976-MS.

Shekhawat DS, Aggarwal A, Agarwal S, Imtiaz M. Magnetic recovery-injecting newly designed magnetic fracturing fluid with applied magnetic field for EOR. In: SPE Asia pacific hydraulic fracturing conference, 24–26 Aug, Beijing, China; 2016. https://doi.org/10.2118/181853-MS.

Socoliuc VM, Vékás L. Hydrophobic and hydrophilic magnetite nanoparticles: synthesis by chemical coprecipitation and physico-chemical characterization. In: Nirschl H, Keller K, editors. Upscaling of bio-nano-processes. Lecture notes in bioengineering. Berlin: Springer; 2014.

Soleimani H, Baig MK, Yahya N, Khodapanah L, Sabet M, Demiral BMR, et al. Synthesis of ZnO nanoparticles for oil–water interfacial tension reduction in enhanced oil recovery. Appl Phys A. 2018;124(2):128. https://doi.org/10.1007/s00339-017-1510-4.

Starowicz M, Starowicz P, Żukrowski J, Przewoźnik J, Lemański A, Kapusta C, et al. Electrochemical synthesis of magnetic iron oxide nanoparticles with controlled size. J Nanopart Res. 2011;13(12):7167–76. https://doi.org/10.1007/s11051-011-0631-5.

Torsater O, Engeset B, Hendraningrat L, Suwanro S. Improved oil recovery by nanofluids flooding: an experimental study. In: SPE Kuwait international petroleum conference and exhibition, 10–12 Dec, Kuwait City, Kuwait; 2012. https://doi.org/10.2118/163335-MS.

Tsai T, Kuo L, Chen P, Lee D, Yang C. Applications of ferro-nanofluid on a micro-transformer. Sensors. 2010;10(9):8161–72. https://doi.org/10.3390/s100908161.

Wu W, He Q, Jiang C. Magnetic iron oxide nanoparticles: synthesis and surface functionalization strategies. Nanoscale Res Lett. 2008;3(1):397–415. https://doi.org/10.1007/s11671-008-9174-9.

Yu H, Kotsmar C, Yoon KY, Ingram D, Johnston KP, Bryant SL, et al. Transport and retention of aqueous dispersions of paramagnetic nanoparticles in reservoir rocks. In: SPE improved oil recovery symposium, 24–28 Apr, Tulsa, Oklahoma; 2010. https://doi.org/10.2118/129887-MS.

Zeyghami M, Kharrat R, Ghazanfari M. Investigation of the applicability of nano silica particles as a thickening additive for polymer solutions applied in EOR processes. Energy Sources Part A. 2014;36:1315–24. https://doi.org/10.1080/15567036.2010.551272.

Zhang T, Murphy M, Yu H, Bagaria HG, Yoon KY, Neilson BM, et al. Investigation of nanoparticle adsorption during transport in porous media. SPE J. 2015;20:667–77. https://doi.org/10.2118/166346-PA.

Zhang T, Murphy M, Yu H, Huh C, Bryant SL. Mechanistic model for nanoparticle retention in porous media. Transp Porous Med. 2016;115(2):387–406. https://doi.org/10.1007/s11242-016-0711-1.